RSC Advances

ROYAL SOCIETY OF CHEMISTRY

www.rsc.org/advances

Reduction chemical reaction synthesized scalable 3D porous silicon/carbon hybrid architectures as anode materials for lithium ion battery with enhanced electrochemical performance

Qun Li[a] and Longwei Yin*[a], Xueping Gao*

Key Laboratory for Liquid-Solid Structural Evolution and Processing of Materials, Ministry of Education, School of Materials Science and Engineering, Shandong University, Jinan 250061, P. R. China

Email: yinlw@sdu.edu.cn, xpgao@sdu.edu.cn

ABSTRACT: We report on a scalable fabrication of 3D interconnected porous silicon/carbon (Si/C) hybrid architectures via a controllably magnesiothermic reduction route from silica aerogels. The molten magnesium, as a reducing agent, can easily flow into the pores of silica aerogels, and reacts with the silica aerogels to form nanocrystalline Si. The Si nanocrystals can grow into Si nanosheets and assemble into the 3D interconnected hierarchically porous Si architectures, due to the large negative enthalpies associated with magnesiothermic reduction. The pulverization and cracking effect caused by large volume change during cycling and the unstable solid-electrolyte interphase can be greatly alleviated using the 3D porous hierarchical Si/C hybrid architectures as anode materials for lithium ion batteries (LIBs). The 3D porous Si/C hybrid architectures exhibit significantly improved electrochemical performance of high reversible capacity, high-rate capability, and excellent cycling performance as anode electrode materials for LIBs. The 3D porous Si/C hybrids display an improved electrochemical performance as anodes for LIBs, showing an excellent reversible capacity of 1552 mA h g^{-1} and a Coulombic efficiency nearly 100% after 200 cycles at a current density of 200 mA g^{-1}, and demonstrating a greatly enhanced rate capability of a reversible capacity of 1057 mA h g^{-1} even after 50 cycles at current density of 2.0 A g^{-1}. The outstanding cycling performance and rate capability of the 3D porous hierarchical Si/C hybrid anodes can be attributed to the advantage of 3D interconnected porous structure, carbon layer volume buffering effect, and the good carbon conductive network.

KEYWORDS: three-dimensional porous silicon, silica aerogel, silicon nanosheet, anode material, lithium ion battery

1. Introduction

In the past few years, silicon (Si) has attracted particular attention as anode materials for lithium ion batteries (LIBs) because of its high theoretical capacity and abundant resources.[1-3] Si can theoretically accept 4.4 Li^+ ($Li_{4.4}Si$) per atom, leading to a capacity of 4200 mA h g^{-1}, which is an order of magnitude higher than that of conventional graphite materials. However, the main obstacles for further performance improvement and potential application of Si anodes for LIBs are that the large volume change formed (>300%) during lithium insertion/extraction cycles, and low electrical conductivity of Si anode materials. In order to overcome these drawbacks, several strategies have been taken to enhance capacity and cycling stability of Si electrodes. It has been demonstrated that nanostructured Si materials such as nanoparticles,[4] nanocable arrays,[5] nanowire,[6-10] and nanotubes,[11,12] could greatly enhance the cycling life, specific capacity and rate capability. However, the electrochemical performance of the Si nanostructured materials is still not satisfied. Furthermore, the microstructures and yields of the most reported Si nanostructures synthesized by chemical vapor deposition (CVD) or physical vapor deposition route are difficult to control, which needs higher temperature, vacuum and poisonous gas precursor.[13,14]

Recently, porous structured Si materials have attracted much attention as anode materials for LIBs. Porous structures can alleviate the volume change during lithium insertion/extraction process, shorten the lithium ion transfer path, and provide sufficient contact and enhance charge transfer at the interface between the electrode and the electrolyte.[15-20] Chemical etching methods, such as wet chemical etching, electrochemical etching, and metal-assisted chemical etching, have been used to fabricate porous Si materials.[21] However, only a yield of 30-40% porous Si can be obtained for the chemical etching route. Template strategy is another important route to prepare porous Si materials. The silica sphere synthesized by Stöber method is used usually to prepare 3D porous Si materials as templates and reactants.[22,23] The synthesized 3D hierarchically porous Si materials facilitate a faster transport of lithium ions, better intercalation kinetics, and remarkably enhanced specific capacity at high current density.

A magnesiothermic reduction route was developed to synthesize porous Si from silica precursors. It is shown that the porous Si could be recycled from the rice husk and diatomaceous earth containing the Si elements.[24-27] Bao et al. demonstrated that 3D porous Si materials could be synthesized from silica under a low temperature through a reduction chemical reaction.[27] The tedious pre-processing is a critical factor to influence the microstructures, surface area and crystalline state of porous Si using the rice husk and diatomaceous earth as the Si precursor. For 3D porous pure Si anode materials, further performance improvement is greatly hampered by the unstable SEI layer formed between Si and electrolytes,[2,12] cracking and pulverizing effects related to the large

stress and strain from the volume changes generated during lithiation-delithiation process, and inherent low electronic conductivity of Si. To fully make use of both merits of Si and carbon materials, such as long cycle life, high electron conductivity of carbon and high lithium-storage capacity of Si, it is a general and effective way to design 3D porous Si/C nano-hybrid architectures to improve the electrochemical performance of Si anode materials. Carbon nanotube,[28] graphene,[29] and carbon cloth[7] were reported to be combined with Si to form the 3D Si/C hybrids, displaying outstanding higher Coulombic efficiency, better capacity retention ability and rate capability. It is proved that the introduction of carbon in Si can provide a rapid lithium transport pathway, reduce the cell impedance and stabilize the electrode structure during charge/discharge cycles. While the reported 3D Si/C hybrids display improved electrochemical performance, the most challenge for the potential industrial application of Si-based anode materials is a scalable and structure controllable production of Si/C hybrids at a low cost.

Herein, we report on a scalable production of 3D porous interconnected Si/C hybrids via a controllably magnesiothermic reduction route from silica aerogels. The 3D porous Si/C hybrids show an excellent electrochemical performance as anode materials for LIBs, displaying an excellent reversible capacity of 1552 mA h g^{-1} and a Coulombic efficiency nearly 100% after 200 cycles at a current density of 200 mA g^{-1}. The Si/C hybrid anodes demonstrate an enhanced rate capacity of 1057 mA h g^{-1} even after 50 cycles at a current density of 2.0 A g^{-1}. The excellent specific capacity, stable cycle performance and superior rate capability of this hybrid material can be ascribed to the rich porous channels and the good carbon conductive network.

2. Experimental

2.1 Preparation of silica aerogels, porous Si and Si/C hybrids

Silica gels were prepared by the acid-catalyzed sol-gel method using TEOS. 10 mL TEOS was diluted in a mixture of 20 mL ethanol and 4 mL water under stirring for half an hour to form clear solution, and then the hydrogen chloride (HCl) aqueous solution (0.2 mol L^{-1}) was added to adjust the pH value to 3 and initiated the hydrolysis reaction. Then ammonia aqueous solution was added to adjust the pH value to 7 after stirring at room temperature for 4 h, and the polycondensation and gelation of the hydrolyzed species were carried out at the same time. After 24 h of aging to strengthen the gel network structure, the as-prepared gel was subjected to solvent exchange with ethanol for three times in 24 h, followed by solvent exchange with n-hexane for three times in 24 h. The silylation of the gels was then performed with chlorotrimethylsilane diluted in n-hexane. Finally, the treated gel was directly dried at 100 ^{o}C for 12 h to produce silica gel materials.[30]

0.2 g silica aerogel and 0.2 g magnesium powder were blended simply and put in a corundum boat, and then

heated in a tube furnace at 650 ^{o}C with a temperate rate of 5 ^{o}C min^{-1} for 5 h under Ar atmosphere. The obtained powders were soaked in HCl solution to remove MgO. 0.073 g resorcinol and 0.16 g formaldehyde (37 wt%) were added to 0.5 g H_2O, and 0.108 g sodium carbonate aqueous solution (5 mM L^{-1}). The mixture was stirred for 10 min to ensure resorcinol dissolve. 0.2 g porous Si were put into the mixture and then ultrasonic for 2 h. The samples were treated at room temperature, 50 ^{o}C and 90 ^{o}C for 1 day, respectively. After the polymerization was completed, the samples was thermally treated at 900 °C for 3 h for the carbonization under Ar atmosphere.[31-32]

2.2 Structure and electrochemical characterization

The crystal structure information of the synthesized samples was established by powder X-ray diffraction (XRD, Rigaku D/Max-KA diffractometer with Cu Ka radiation). X-ray photoelectron spectroscopy (XPS, ESCALAB 250 with 150 W Al Ka probe beam) was used to characterize the chemical composition information. Raman spectroscopy was measured and collected using a JY HR800 micro Raman spectrometer. SU-70 field emission scanning electron microscopy (FESEM) and transmission electron microscopy (TEM Tecnai 20U-TWIN) were employed to analyze the microstructures of the synthesized products. The specific Brunauer-Emmett-Teller (BET) surface area was determined by N_2 adsorption/desorption on a V-Sorb 2800 series analyzer (Gold APP Co. Ltd.). Thermogravimetric analysis (TGA) was carried out under a flow of air with the temperature ramp of 10 °C min^{-1} from 40 to 800 °C using thermogravimetric analyzer (SDTQ600).

The electrochemical measurements were conducted using standard 2025 type coin cells with copper foil as the current collectors, lithium foil as counter electrode and reference electrodes and 1.0 M $LiPF_6$ in a 1:1 (V/V) mixture of ethylene carbonate (EC) and diethyl carbonate (DEC) as the electrolyte, plus 2 wt.% vinylene carbonate (VC). The cutoff voltage window is 0.01-2.0 V. The working electrode mixture slurry was prepared by mixing 60 wt% active materials, 20 wt% acetylene carbon black, 20 wt% binder (styrene butadiene rubber/sodium carboxymethyl cellulose, 1:1 by weight), and an adequate amount of H_2O. Galvanostatically cycled test was carried out on a LAND CT2001A instrument (Wuhan, China) at room temperature. Electrochemical workstation (PARSTAT2273) was used to study cyclic voltammetry (CV) test in a potential window of 0.01-3.00 V at a scan rate of 0.1 mV s^{-1}.[33] Electrochemical impedance spectroscopy (EIS) measurements were performed in the frequency between 100 kHz and 10 mHz and the amplitude is 5 mV.[33]

3. Results and discussion

3.1 XRD characterization of the Si/C hybrids

Fig. 1 shows the powder XRD patterns of the silica aerogels, porous Si and Si/C hybrid materials. The presence of the broad diffraction peak at 22.5^{o} of SiO_2 suggests that the synthesized SiO_2 aerogels are in an amorphous

state. For the magnesiothermic reduction synthesized porous pure Si samples, the sharp diffraction peaks at 28.3, 47.2, 56.1, 69.0, and 76.2^{o} can be assigned to (111), (220), (311), (400) and (331) planes of a cubic structure (space group: *Fd-3m*) (JCPDS: 27-1402), respectively.[34] This shows that magnesiothermic reduction is effective to fabricate highly crystalline porous Si materials. For the Si/C hybrids, after the carbon coating via carbonization process, the peak position and shape are basically in agreement with that of the pure Si materials, indicating that the pyrolysis does not change the original crystalline structure of Si. There are some very weak peaks at 35.8, 41.8, and 71.5^{o} in XRD patterns, corresponding to the (131), (112), and (431) planes of Mg_2SiO_4. Apart from MgO, there are some by-products of Mg_2Si and Mg_2SiO_4 in magnesiothermic reduction action. As we all known, MgO and Mg_2Si could be removed easily with HCl, whereas a small amount of Mg_2SiO_4 will retain in the Si matrix.[35] Fig. S1 depicts the optical images of the silica aerogels, reduction reaction obtained porous Si, and the Si/C hybrids. It is shown that yield of the Si/C hybrids is scalable, and the color of the loose flocculating products takes an evolution from white of silica aerogel, to brownish for Si, and finally to the black for the Si/C hybrids.

3.2 XPS and Raman characterization of the Si/C hybrids

X-ray photoelectron spectroscopy (XPS) was used to further characterize the chemical composition and chemical bonding state of synthesized porous Si/C sample products. Fig. 2a displays an overall XPS spectrum for peaks of Si (Si 2s, Si 2p), O (O 1s), and C (C 1s) elements. Fig. 2b depicts a XPS spectrum of C 1s, a symmetrical peak at 284.8 eV corresponding well to amorphous carbon structure.[34] Another symmetrical peak observed for O 1s located at 532.9 eV (Fig. 2c) can be assigned mainly to oxide layer of SiO_2. From XPS spectrum (Fig. 2d) of deconvoluted Si 2p, it suggests that three peaks locate at 100.1 eV, 101.5 eV and 103.3 eV, respectively. The lower energy component at 100.1 eV can be assigned to Si-H bond.[35] The stronger peak at 101.5 eV is assigned mainly to Si-Si bond. The peak at 103.3 eV is attributed to the Si-O band presented in the synthesized Si/C products.[36-39]

The Raman spectra of the porous Si and Si/C hybrids are shown in Fig, 2e and 2f. Two peaks are observed at 508 and 928 cm^{-1} for pure porous Si sample, respectively (Fig. 2e). The two strong peaks at 508 cm^{-1} and 928 cm^{-1} are attributed to crystalline Si. As for Raman spectrum of the Si/C hybrids (Fig. 2f), besides two peaks located at 508 and 928 cm^{-1}, two additional peaks at 1356 and 1586 cm^{-1} were observed, which are attributed to the D (disordered) band and the G (graphite) band of carbon, respectively. For the graphitization degree of the carbon, it is generally evaluated according to the ratio of the intensity of the D band to G band (I_D/I_G). The ratio of intensity between I_D and I_G band is 0.95, indicating that a low graphitization degree for the Si/C hybrids.[34]

3.3 SEM and TEM characterization of the Si/C hybrid samples

The microstructures of the synthesized products are observed by field emission scanning electron microscopy (FE-SEM). The microstructures of the silica aerogels are illustrated in Fig. S2, showing that the silica aerogels are

composed of silica spheres interconnected each other. In order to synthesize desirable 3D porous Si architectures from silica aerogels, a magnesiothermic reduction was carried out at 650 ℃ for 5 h. Figure 3a-3c depicts the FE-SEM images of the magnesiothermic reduction route synthesized porous Si samples. It is shown that the obtained Si products display a characteristic of 3D interconnected porous framework. From a magnified FESEM image in Fig. 3d, it is revealed that the synthesized 3D porous Si architectures are composed of Si nanosheets interconnected each other, forming the typical 3D porous interconnected Si architectures. It is shown that the silica aerogels have been successfully transformed to 3D porous Si architectures via the controllably magnesiothermic reduction reaction. The 3D porous structure of Si architectures can offer the sufficient space to buffer the volume expansion of Si anode materials during charge and discharge process. On the other hand, the porous interconnected channel can shorten the path for lithium ion transport, improving the lithium ion storage performance remarkably.

Transmission electron microscopy (TEM) is applied to further investigate the detailed microstructures of the synthesized porous Si materials, as shown in Fig. 4. From low- and high-magnification TEM images in Fig. 4a, the 3D porous interconnected architectures for the synthesized Si products can be identified. The synthesized 3D porous Si products are composed of Si nanosheets interconnected with each other, forming the porous interconnected 3D architectures. A typical high-magnification TEM image for the interconnected Si nanosheets is shown in Fig. 4b. A HRTEM lattice image for the Si nanosheet in Fig. 4c clearly suggests that the Si nanosheet is single crystalline, the upper left side is a Fourier transform electron diffraction pattern from [-111] zone axis corresponding to the HRTEM lattice image. The d-spacings of 0.19 nm (Fig. 4d) are in good well agreement with that of (02-2) and (202) planes of Si, clearly indicating the single crystalline nature of the Si nanosheets. A thin amorphous layer about 0.4-0.5 nm on the surface of the Si nanosheet can be related to a thin layer of silica. Fig. 5a shows a low resolution TEM image of the Si/C hybrids. Compared with the porous pure Si samples in Fig. 4a, two distinctive phases with different color contrasts can be revealed, with carbon layer coated on the surfaces of Si. The detailed microstructure information for the Si and C can be shown more clearly in Fig. 5b. The carbon layer coated on the surface of Si is in a range of 3-4 nm, the marked 0.35 nm corresponds well to d-spacing of (002) plane of graphite.

Fig. S3 shows the thermogravimetry analyses (TGA) curve of the porous Si and Si/C hybrids, which was obtained under air from 40 to 800 °C with a temperature ramp of 10 °C min^{-1}. When the temperature increased to 300 °C, the pure porous Si started to be oxidized, and the increase of the sample mass can be calculated to be about 2.5 wt%. The crystal Si in Si/C hybrids can also be oxidized partly after carbon disappearing. According to the TGA results, the content of carbon in the Si/C hybrid can be estimated to be about 10.9 wt%.

The formation mechanism of the porous 3D interconnected Si/C hybrid samples can be illustrated in Schema 1. Silica aerogels with large surface area and pores are used as a suitable Si source (Schema. 1a). Magnesium is used as a reducing agent to transform silica to Si. At a temperature of 650 ℃, the molten magnesium can easily flow and diffuse into the porous sites of silica aerogels, and react with silica aerogels to form the Si-MgO nanocomposite (Schema 1b).[27,35] The chemical reaction can be described as:

$$2Mg\ (s) + SiO_2\ (s) = Si\ (s) + 2MgO\ (s) \quad (1)$$

Due to the large negative enthalpies associated with magnesiothermic reduction, a large quantity of heat can be released. The Si nanocrystals will self-aggregate together at a higher temperature condition, as shown in Schema 1c. Then, the magnesiothermic reduction-route fabricated Si nanocrystals can grow into Si nanosheets and assemble into the interconnected porous hierarchical Si framework nanostructures (Schema 1d).[24-25,35] The formed Si/MgO nanocomposites are further treated by an etching process using HCl solution to remove MgO.[24] The interconnected porous structure composed of Si nanosheets was formed after removing MgO, as shown in Schema 1e. Subsequently, a homogeneous carbon layer coating on surface of hierarchical Si nanostructures was realized via a polymerization process of a mixture of resorcinol and formaldehyde (Schema 1f).

3.4 Nitrogen adsorption-desorption isotherm characterization of the Si/C hybrids

The nitrogen adsorption-desorption isotherms and the corresponding pore size distribution curves obtained by the Barrett-Joyner-Halenda (BJH) method of the silica aerogels, porous Si and Si/C hybrids are shown in Fig. 6. It is shown that these three curves show a similarly typical characteristic of IV type with an obvious capillary condensation step, indicating that a mesoporous nature.[34] The textual parameters including BET specific surface area, pore diameter, pore volume of the porous Si and Si/C hybrids are summarized in Table 1. The specific surface area of the silica areogels can reach about 1038.8 $m^2 g^{-1}$, while the specific area of the porous Si samples decreases to 107.1 $m^2 g^{-1}$ (Fig. 6a and 6b). The porous Si/C hybrid samples can reach a high specific surface area of 126.7 $m^2 g^{-1}$ (Fig. 6c). For the evolution of pore size distribution, the average pore diameter increases from 30.2 nm for silica aerogel to 34.2 nm for porous Si, and finally to 21.8 nm for the Si/C hybrids.[25,35]

3.5 Electrochemical characterization of the Si/C hybrids

To understand the electrochemical reaction of the synthesized Si/C samples, the cyclic voltammetry (CV) curves for the first five cycles of the samples were investigated at a scan rate of 0.1 mV s^{-1} in a voltage range of 0.01-3.00 V versus Li/Li^+ (Fig. 7a). In the case of the first cathodic half-cycle, two reduction peaks located at 0.5 V and 0.03 V are observed, respectively. The broad cathodic peak at around 0.5 V could be attributed to the formation of a SEI film,[35] such a peak disappearing in the subsequent cycles. Another cathodic peak appearing at 0.03 V can be ascribed to the formation of a series of Li_xSi alloys. In the case of the first anodic process, a broader

anodic peak at about 0.3 V corresponds to the dealloying process of the Li_xSi alloys.[8,39] After the first cycle, the CV curves of the Si/C electrodes in the second cycle remain similar to the first cycle, and the curves after the second cycle are nearly overlapped, suggesting an excellent cycle performance of the electrodes.

The electrochemical impedance spectroscopy (EIS) was used to investigate the charge transport kinetics of the Si/C hybrid electrode samples. Fig. 7b shows the Nyquist profiles of the AC impedance for pure Si and Si/C samples, which were measured at an open circuit voltage state using fresh cells. In the EIS spectra, both the pure porous Si electrode and Si/C hybrid electrode show one depressed semicircle in high frequency and a straight line portion in low frequency range. The inset in Fig. 7b is the equivalent circuit. R_e is the resistance for lithium ion transport in the electrolyte. R_f is the resistance for lithium ion migration through the SEI film. R_{ct} represents charge-transfer impedance at electrode-electrolyte interface, and the Warburg impedance (W) is related to lithium ions transfer process in solid electrode materials.[34] The data on charge-transfer resistance of the electrodes are calculated and listed in Table 2. Obviously, the Nyquist plot for the Si/C sample reveals a lower R_{ct} value (~234.7 Ω cm^2) at high frequency than pure Si sample (~502.1 Ω cm^2), indicating a smaller electrochemical reaction resistance for Si/C hybrid electrode during lithium ion insertion/extraction process. The resistance for lithium ion migration through SEI film of the Si/C hybrid (~515.4 Ω cm^2) is also smaller than that of pure porous Si (~5796.2 Ω cm^2), suggesting a stable SEI film is formed for the Si/C hybrid sample. The EIS results indicate that the introduction of carbon layer can facilitate the charge transfer during the lithium insertion/extraction processes, favorable for improving the cycle performance and rate capability of the 3D porous Si/C hybrid electrodes.

To examine the electrochemical performance of the synthesized Si/C hybrid samples as anode materials for LIBs, the discharge-charge profiles of the Si/C hybrid anode materials was investigated. Fig. 7c and 7d shows profiles for the voltage versus capacity of the 1st, 2nd, 5th, 10th, and 50th cycle of the synthesized samples at a voltage window from 0.01 V to 2.00 V at a current density of 200 mA g^{-1}. For the pure Si sample (Fig. 7c), the first discharge and charge capacity are 3811 mA h g^{-1} and 2717 mA h g^{-1}, respectively, corresponding to a Coulombic efficiency of about 71.3%. As for the Si/C hybrid sample (Fig. 7d), the first discharge and charge capacity are 3455 mA h g^{-1} and 2265 mA h g^{-1}, respectively, with a Coulombic efficiency of about 65.7%. Although the initial reversible capacity and initial Coulombic efficiency of the Si/C hybrids are lower than that of pure Si samples, in the subsequent cycles, the reversible capacity of the Si/C hybrids decreases slowly and remains relatively more stable compared with that of pure Si samples. At the tenth cycle, the porous Si/C hybrid architectures and pure porous Si samples display a reversible specific capacity of 1699 and 1546 mA h g^{-1}, and Coulombic efficiency of 99.4% and 97.5%, respectively. After 50 discharge-charge cycles, the Si/C hybrid anode exhibits a high reversible capacity of 1583 mA h g^{-1} and a Coulombic efficiency of almost 100% from an initial

Coulombic efficiency of 65.6%. In contrast, the pure Si electrode only exhibits a reversible capacity of 1049 mA h g^{-1} and a Coulombic efficiency of 98.8%. This indicates that the Si/C hybrid electrode displays a much higher reversible capacity and perfect cycling stable performance than that of the pure porous Si electrode. From Fig. 7c and 7d, it is shown that both the pure porous Si and Si/C hybrid electrodes display two plateaus in the first discharge. One is in range from 1.30 V to 0.75 V, corresponding to the formation of SEI on the Si surface. This plateau disappears in the next cycles. The other long flat plateau is below 0.1 V, which is associated with the lithium-alloying process of crystalline Si to form an amorphous Li_xSi phase. In the charge process, a charge plateau at about 0.5 V is assigned to the dealloying process of the Li_xSi alloys.

The cycle capacity and the stability of the porous Si, porous Si/C hybrid and commercial micro-powder Si (< 1 μm) lithium-ion battery anodes are comparatively investigated using a galvanostatic technique. Fig. 8 shows the capacity performance and rate capacity curves, Coulombic efficiency of these synthesized samples. The Si/C hybrid samples demonstrate the greatly improved electrochemical performance compared with pure 3D porous Si and commercial Si powder samples. The Si/C hybrid anode displays an initial discharge and charge capacity of 3455 mA h g^{-1} and 2269 mA h g^{-1}, respectively, showing a Coulombic efficiency of about 65.7%. In the first 10 cycles, the reversible capacity of the 3D Si/C hybrid anode decreases relatively faster from 2269 to 1695 mA h g^{-1}, and then decreases gradually to 1575 mA h g^{-1} at the 20th cycle. After reaching to 1575 mA h g^{-1} at the 20th cycle, the reversible capacity of the 3D porous Si/C hybrid anodes remain almost stable. After 200 cycles, the reversible capacity of the Si/C hybrid sample still maintains a high value of 1552 mA h g^{-1}. For the Coulombic efficiency of the Si/C hybrid sample, it can reach 98% after 5 cycles, even though the initial Coulombic efficiency is 65.6%, relatively lower, and remains as nearly 100% after 10 cycles, as shown in Fig. 8c and 8d.

The first discharge and charge capacity of the commercial Si micro-powder are 2996 mA h g^{-1} and 2617 mA h g^{-1}, respectively, showing a Coulombic efficiency of 87.3%. However, the reversible charge capacity decreases quickly to 316.9 mA h g^{-1} after 10 cycles, which is due to the particle pulverization resulted from the huge volume changes during the lithium insertion/extraction process. It is the reason that the commercial micro-powder Si can not be directly used as anode mateials for LIBs in industry application.

As for the 3D porous pure Si sample, the first discharge and charge capacity are 3811 mA h g^{-1} and 2717 mA h g^{-1}, respectively, with a Coulombic efficiency of 71.3%. It is noted that SiO_2 aerogels can be converted into porous Si almost via magnesiothermic reduction rout, though a certain amount of SiO_2 will still be existed in the porous Si material, as shown in the TEM image of Fig. 4. The SiO_2 layer on the Si nanosheet will influence the initial Coulombic efficiency of the porous Si material, which is smaller than that of the commercial Si powder. At the 5th cycle, the reversible capacity is about 1821 mA h g^{-1}, and the Coulombic efficiency increases to 96.2%.

During the subsequent cycling, the reversible capacity decreases quickly to 882 mA h g^{-1} at the 70th cycle. After the 70th cycle, the reversible capacity tends to be stable, making a slight decrease. At the 200th cycle, the reversible capacity can maintain a value of 830 mA h g^{-1}. The Coulombic efficiency of the porous Si is 99.4% after 200 cycles and keeps steady, shown in Fig. 8c.

It is shown that in comparison with the commercial Si powder and the 3D pure porous Si samples, the porous Si/C hybrid sample shows a higher capacity and a better cycle stable performance. Bulk Si anode material demonstrates the poor cycling performance, due to the pulverization and cracking effect caused by large volume change during cycling. The charge capacity of the bulk electrode material is 2616 mA h g^{-1} at 1st cycle, 668 mA h g^{-1} at 5th cycle, and the reversible charge capacity decreases quickly to 316 mA h g^{-1} after 10 cycles, with a capacity retain of only 12%. It means that the battery composed of the bulk Si material will fail quickly after dozens of cycles. The 3D porous Si/C hybrid anodes exhibit the outstanding cycling performance. The charge capacity of the porous Si/C electrode is 2265 mA h g^{-1} at 1st cycle, 1823 mA h g^{-1} at 5th cycle, and 1693 mA h g^{-1} at 10th cycle, respectively. After 200 cycles, the reversible capacity of the Si/C hybrid sample still maintains a high value of 1552 mA h g^{-1}, with a capacity retain of 68%. Furthermore, further investigation on the longer cycle and higher rate performance of the porous Si/C hybrid electrode at the current density of 1 A g^{-1} shows that the Si/C hybrid electrode can still retain a capacity of more than 1134 mA h g^{-1} after 400 cycles, as shown in Fig S4. Compared with these previous reports, the Si/C hybrids demonstrate superior cycle performance and high rate capability.

Our results demonstrated the high reversible capacity and long cycle stability for the Si/C hybrids, which is comparable with other Si/C composites obtained by CVD and electrochemical etching method. Yushin et al.[40] designed a CVD synthesis process for Si nanoparticles on the surface of carbon-black nanoparticles. This composite anodes demonstrated a discharge capacity of about 1500 mA h g^{-1} at a current density of 1C (372 mA g^{-1}) after 100 cycles. Thakur et al.[41] synthesized a freestanding macroporous silicon film by electrochemical etching of p-type silicon wafers. After being mixed with polyacrylonitrile (PAN) and pyrolyzed, these macroporous Si/C particulates exhibited a capacity of 1000 mA h g^{-1} at a current density of C/5 for over 300 cycles. However, the microstructures and yields of these Si nanostructures by chemical vapor deposition route are difficult to control, which needs higher temperature, vacuum and poisonous gas precursor.

Compared with the porous Si anodes obtained from magnesiothermic reduction in the previous reports, our results demonstrates the higher capacity and longer cycle life. For example, Shen et al.[26] synthesized porous silicon anode material by magnesiothermically reducing diatomaceous earth, displaying a capacity of 633 mA h g^{-1} at a current density of 0.2 mA cm^{-2} after 30 cycles. Wang et al.[39] prepared silicon/carbon nanocomposite

exhibits a reversible capacity of 678 mA h g^{-1} after 50 cycles at a current density of 100 mA g^{-1}. Three-dimensional mesoporous silicon reported by Jia et al.[35] displayed a stable capacity of 1500 mA h g^{-1} at a current density of 1C (372 mA g^{-1}) for 100 cycles. The mesoporous silicon nanorod demonstrates reversible specific capacity of 1038 mA h g^{-1} after 170 cycles at a current density of 200 mA g^{-1}.[8]

To investigate the rate capability of the 3D porous Si/C hybrid anodes, the Si/C hybrid anodes are cycled for each ten cycles under an increasing current density from 0.1 A g^{-1} to 2.0 A g^{-1} (Fig. 8b). In the first ten cycles at a current density of 0.1 A g^{-1}, the reversible capacity of the Si/C hybrid anode rapidly decreases with the cycle time increasing, displaying a reversible capacity of 2158 mA h g^{-1} at the 10th cycle. Subsequently, the reversible capacity of the 3D porous Si/C hybrid anode shows a reversible capacity of 1496 mA h g^{-1} at a current density of 0.5 A g^{-1} after 30 cycles, and 1057 mA h g^{-1} at a current density of 2.0 A g^{-1} after 50 cycles. As the current density is set back to 0.1 C, the capacity is able to return to more than 2413 mA h g^{-1}. The pure porous Si anode shows a reversible capacity of 2051 mA h g^{-1} at a current density of 0.1 A g^{-1} after 10 cycles, 946.9 mA h g^{-1} at a current density of 0.5 A g^{-1} after 30 cycles, 303 mA h g^{-1} at a current density of 2.0 A g^{-1} after 50 cycles, respectively. As the current density returns back to 0.1 A g^{-1}, the reversible capacity can reach 2305 mA h g^{-1}. It is shown that in comparison the rate capability of the 3D porous Si/C hybrid samples show greatly improved rate capability, and should be a great potential as an anode material in LIBs.

The remarkable electrochemical performance, especially the high specific capacity and enhanced cycling stability of the Si/C hybrid could be attributed to the synergistic interaction between porous Si structure and carbon layer, as shown in Schema 2. (1) EIS spectra indicate that well-distributed carbon coating layer on the Si surface improves the electrical conductivity and the charge transfer kinetics of Li^+ ions at the interface between the electrolyte and electrode. (2) The elastic nature of carbon layer coating on the surfaces of Si, renders the Si/C hybrids very effective in accommodating the volume strain. (3) The open pore system with interconnected pore channels would facilitate the accessibility of the electrolyte, and could promote lithium ion diffusion. The porous structure offers sufficient void space to alleviate the huge volume expansions of the Si, enhancing the capacity performance and the Coulombic efficiency of the porous Si electrode. Bare porous Si can not avoid pulverization after many cycles, as shown in Schema 2. (4) This hierarchically porous structure composed of Si nanosheet tightly interconnected to form three dimensional channels can effectively take the advantages of both the high specific capacity from nanoscale Si and good stability from hierarchical structure. The hierarchical porous structures not only provide an elastic buffer space to accommodate the volume expansion/contraction of Si during Li+ ions insertion/extraction process, but also efficiently prevent the aggregation of Si nanosheet and the cracking or crumbling of electrode material upon continuous cycling, thus maintaining large specific capacity, good

coulombic efficiency, high rate capability and cycling stability.

4. Conclusions

In summary, scalable 3D porous Si/C hybrid materials with interconnected channels are synthesized via a facile magnesiothermic reduction method using silica aerogel as a pristine Si source. Due to the large surface area, porous structures and the large negative enthalpies associated with magnesiothermic reduction, the magnesiothermic reduction-route fabricated Si nanocrystals can grow into Si nanosheet and assemble into the 3D interconnected hierarchically porous Si architectures. The pulverization and cracking effect due to large stress and strain from volume change during cycling and an unstable solid-electrolyte interphase can be greatly alleviated using the 3D hierarchical Si/C hybrid architectures as anode materials for LIBs. The 3D hierarchical Si/C hybrid anodes display an excellent reversible capacity of 1552 mA h g^{-1} after 200 cycles at a current density of 200 mA g^{-1}. The Si/C hybrid anodes also demonstrate improved rate capacity of 1057 mA h g^{-1} at a current density of 2.0 A g^{-1} even after 50 cycles. The excellent rate capability of the Si/C hybrid materials can be ascribed to the rich porous channels and the good carbon conductive network. The porous structure offers sufficient void space to alleviate the huge volume expansions of the Si, which enhance the capacity and the Coulombic efficiency of the porous Si electrode. The carbon layer improves the sample electrical conductivity and promotes the formation of the SEI layer on the surface of porous Si. This new porous Si/C hybrid material with good electrochemical performance can find potential applications as anode material in lithium ion batteries.

Acknowledgements

We acknowledge support from the National Nature Science Foundation of China (No.: 51272137, 51472148), The National Basic Research Program (No.: 2013CB934303), and the Tai Shan Scholar Foundation of Shandong Province.

References

1 H. Wu, and Y. Cui, *Nano Today*, 2012, **7**, 414.

2 M. L. Terranova, S. Orlanducci, E. Tamburri, V. Guglielmotti, and M. Rossi, *J. Power Sources*, 2014, **246**, 167.

3 J. R. Szczech, and S. Jin, *Energy Environ. Sci*., 2011, **4**, 56.

4 L. Xue, G. Xu, Y. Li, S. Li, K. Fu, Q. Shi, and X. Zhang, *ACS Appl. Mater. Interfaces*, 2013, **5**, 21.

5 F. F. Cao, J. W. Deng, S. Xin, H. X. Ji, O. G. Schmidt, L. J. Wan, and Y. G. Guo, *Adv. Mater.*, 2011, **23**, 4415.

6 C. K. Chan, H. Peng, G. Liu, K. Mcilwrath, X. F. Zhang, R. A. Huggins, and Y. Cui, *Nature Nanotech.*, 2008, **3**, 31.

7 B. Liu, X. Wang, H. Chen, Z. Wang, D. Chen, Y. Cheng, C. Zhou, and G. Shen, *Sci. Rep.*, 2013, **3**, 1622.

8 Y. Zhou, X. Jiang, L. Chen, J. Yue, H. Xu, J. Yang, and Y. Qian, *Electrochimica Acta*, 2014, **127**, 252.

9 J. G. Ren, C. Wang, Q. H. Wu, X. Liu, Y. Yang, L. He, and W. Zhang, *Nanoscale*, 2014, **6**, 3353.

10 H. Kim, and J. Cho, *Nano Lett.*, 2008, **8**, 3688.

11 M. H. Park, M. G. Kim, J. Joo, K. Kim, J. Kim, S. Ahn, Y. Cui, and J. Cho, *Nano Lett.*, 2009, **9**, 3844.

12 H. Wu, G. Chan, J. W. Choi, I. Ryu, Y. Yao, M. T. McDowell, S. W. Lee, A. Jackson, and Y. Yang, *Nature Nanotech.*, 2012, **7**, 310.

13 N. Liu, H. Wu, M. T. McDowell, Y. Yao, C. Wang, and Y. Cui, *Nano Lett.*, 2012, **12**, 3315.

14 R. Yi, F. Dai, M. L. Gordin, H. Sohn, and D. Wang, *Adv. Energy Mater.*, 2013, **3**, 1507.

15 B. M. Bang, J. I. Lee, H. Kim, J. Cho, and S. Park, *Adv. Energy Mater.*, 2012, **2**, 878.

16 B. M. Bang, H. Kim, H. K. Song, J. Cho, and S. Park, *Energy Environ. Sci.*, 2011, **4**, 5013.

17 S. Sim, P. Oh, S. Park, and J. Cho, *Adv. Mater.*, 2013, **25**, 4498.

18 J. Cho, *J. Mater. Chem.*, 2010, **20**, 4009.

19 M. Ge, J. Rong, X. Fang, A. Zhang, Y. Lu, and C. Zhou, *Nano Research*, 2013**, 6**, 174.

20 M. Ge, Y. Lu, P. Ercius, J. Rong, X. Fang, M. Mecklenburg, and C. Zhou, *Nano Lett.*, 2014, **14**, 261.

21 Z. Huang, N. Geyer, P. Werner, J. Boor, U. Gösele, *Adv. Mater.*, 2011, **23**, 285.

22 H. Kim, B. Han, J. Choo, and J. Cho, *Angew. Chem. Int. Ed*., 2008, **47**, 10151.

23 A. Esmanski, and G. A. Ozin, *Adv. Funct. Mater*., 2009, **19**, 1999.

24 D. S. Junga, M. H. Ryou, Y. J. Sungc, S. B. Park, and J. W. Choi, *Proc. Natl. Acad. Sci.*, 2013, **110**, 12229.

25 N. Liu, K. Huo, M. T. McDowell, J. Zhao, and Y. Cui, *Sci. Rep.*, 2013, **3**, 1919.

26 L. Shen, X. Guo, X. Fang, Z. Wang, and L. Chen, *J Power Sources*, 2012, **213**, 229.

27 Z. Bao, M. R. Weatherspoon, S. Shian, Y. Cai, P. D. Graham, S. M. Allan, G. Ahmad, M. B. Dickerson, B. C. Church, Z. Kang, H. W. Abernathy III, C. J. Summers, M. Liu, and K. H. Sandhage, *Nature*, 2007, **446**, 172.

28 Y. Fan, Q. Zhang, C. Lu, Q. Xiao, X. Wang, and B. Tay, *Nanoscale*, 2013, **5**, 1503.

29 X. Zhou, X. X. Yin, L. J. Wan, and Y. G. Guo. *Chem. Commun.*, 2012, **48**, 2198.

30 T. Sun, H. Fan, Z. Wang, and Z. Wu, *J. Mater. Sci.*, 2013, **48**, 6713.

31 F. Hao, Z. Zhang, and L. Yin, *ACS Appl. Mater. Interfaces*, 2013, **5**, 8337.

32 Z. Zhang, Z. Li, F. Hao, X. Wang, Q. Li, Y. Qi, R. Fan, and L. Yin, *Adv. Funct. Mater.*, 2013, **24**, 2500.

33 Q. Li, L. Yin, Z. Li, X. Wang, Y. Qi, and J. Ma, *ACS Appl. Mater. Interfaces*, 2013, **5**, 10975.

34 H. Tao, L. Z. Fan, W. L. Song, M. Wu, X. He, and X. Qu, *Nanoscale*, 2014, **6**, 3138.

35 H. Jia, P. Gao, J. Yang, J. Wang, Y. Nuli, and Z. Yang, *Adv. Energy Mater.*, 2011, **1**, 1036.

36 J. Sun, X. Han, X. W. Du, and Y. W. Lu, *Mater. Lett.*, 2005, **59**, 3135.

37 C. Martin, M. Alias, F. Christien, O. Crosnier, D. Bélanger, and T. Brousse, *Adv. Mater.*, 2009, **21**, 4735.

38 J. L. Gómez-Cámer, J. Morales, and L. Sánchez, *J. Mater. Chem.*, 2011, **21**, 811.

39 M. S. Wang, and L. Z. Fan, *J. Power Sources*, 2013, **244**, 570.

40 A. Magasinski, P. Dixon, B. Hertzberg, A. Kvit, J. Ayala, and G. Yushin, *Nat. Mater.*, 2010, **9**, 353.

41 M. Thakur, S. L. Sinsabaugh, M. J. Isaacson, M. S. Wong, and S. L. Biswal1, *Sci. Rep.*, 2012, **2**, 00795.

Figure Captions

Fig. 1 XRD patterns of the silica aerogel, porous silicon and Si/C hybrid samples.

Fig. 2 XPS spectra of Si/C hybrid sample for (a) Survey spectrum, (b) C 1s, (c) O 1s, (d) Si 2p. Raman spectra of (e) Pure porous silicon sample and (f) Si/C hybrid sample, the inset in (f) is the magnified G and D peaks.

Fig. 3 FE-SEM images of the magnesiothermic reduction route synthesized porous Si samples.

Fig. 4 TEM images of pure porous silicon sample. (a) and (b) Low magnification- and (c) High-magnification TEM images of the pure porous silicon. The inset in (c) is electron diffraction pattern. (d) A HRTEM lattice image for the Si nanosheet.

Fig. 5 (a) A low resolution TEM image of the Si/C hybrids. (b) A HRTEM lattice image for the Si/C hybrid.

Schema 1 Schematic illustration of the formation process of the 3D porous Si/C hybrid samples.

Fig. 6 Nitrogen adsorption-desorption isotherms and the corresponding pore size distribution for samples. (a) Silica aerogel sample, (b) Porous silicon sample, and (c) Si/C hybrid sample.

Fig. 7 (a) Cyclic voltammetry curves of the first five cycles for Si/C hybrid sample electrodes at a scan rate of 0.1 mV s^{-1} between 0.01 and 3.00 V. (b) Nyquist plot of the synthesized samples. The discharge-charge profiles of electrodes of (c) Porous silicon sample and (d) Si/C hybrid sample at a current density of 200 mA g^{-1} with a voltage range of 0.01-2.00 V versus Li^+/Li.

Fig. 8 (a) Cyclic performance at a current density of 200 mA g^{-1} with a voltage range of 0.01-2.00 V versus Li^+/Li, (b) Rate performances of the synthesized samples. (c) and (d) Coulombic efficiency of the 3D porous Si and Si/C hybrid sample, respectively.

Schema 2 Schematic illustration of Li-ion insertion-extraction mechanism for the synthesized samples, (a) Porous Silicon, (b) Si/C hybrid sample.

Table 1. Textural parameters of the silica aerogel, porous silicon and Si/C hybrid

Sample	BET surface area [m^2g^{-1}]	Average pore diameter [nm]	Porous volume [cm^3g^{-1}]
Silica aerogels	1038.8	30.2	4.7
Porous silicon	107.1	34.2	0.6
Si/C hybrid	126.7	21.8	0.2

Table 2 EIS fitted parameters for porous Si and Si/C hybrid sample

Sample	R_e ($\Omega \cdot cm^2$)	R_{ct} ($\Omega \cdot cm^2$)	R_f ($\Omega \cdot cm^2$)
Porous silicon	3.6	502.1	5796.2
Si/C hybrid	2.9	234.7	515.4

Fig. 1

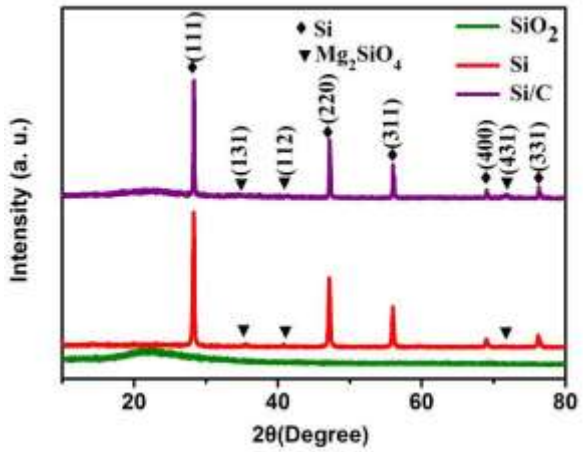

Fig. 2

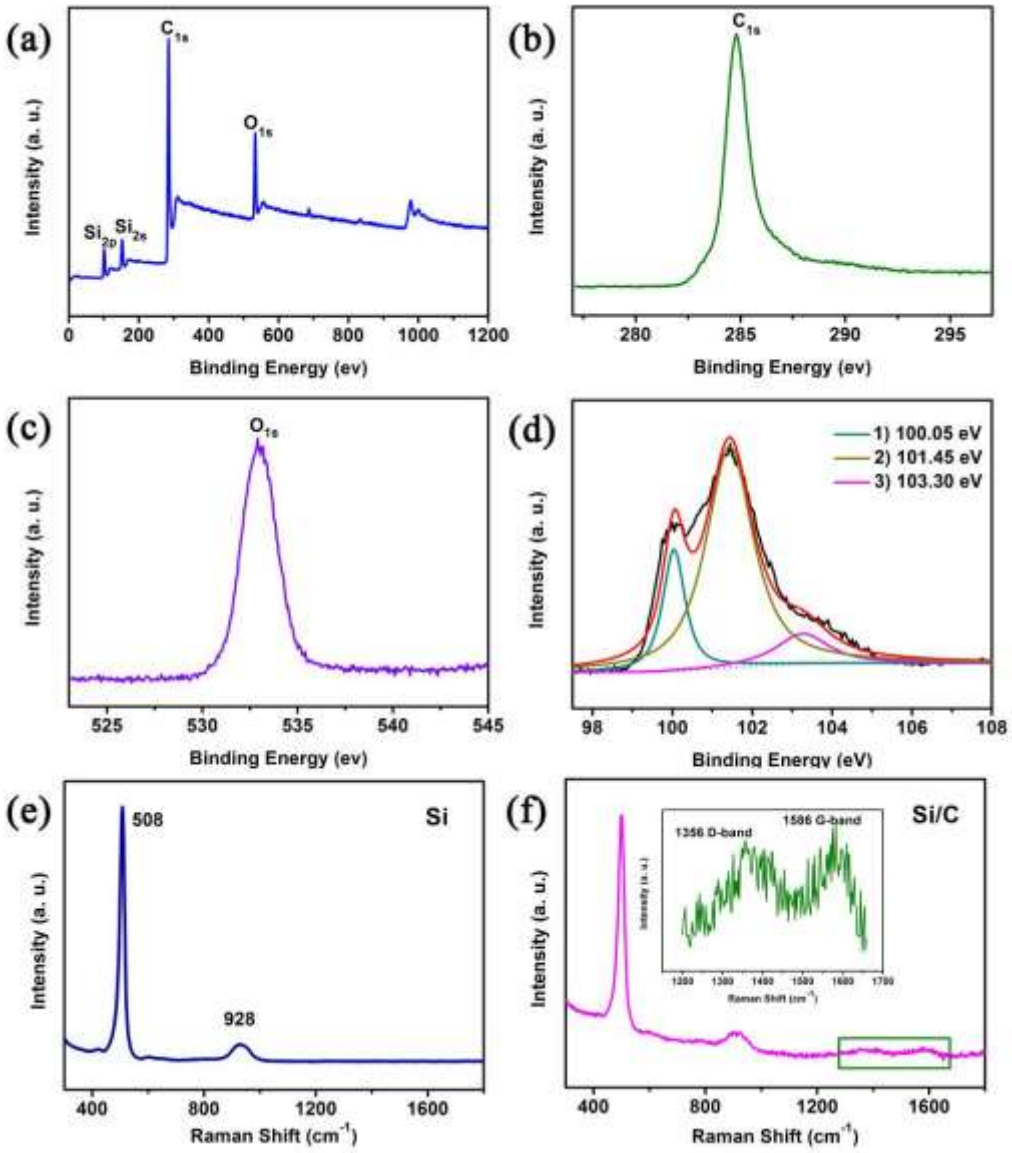

Fig. 3

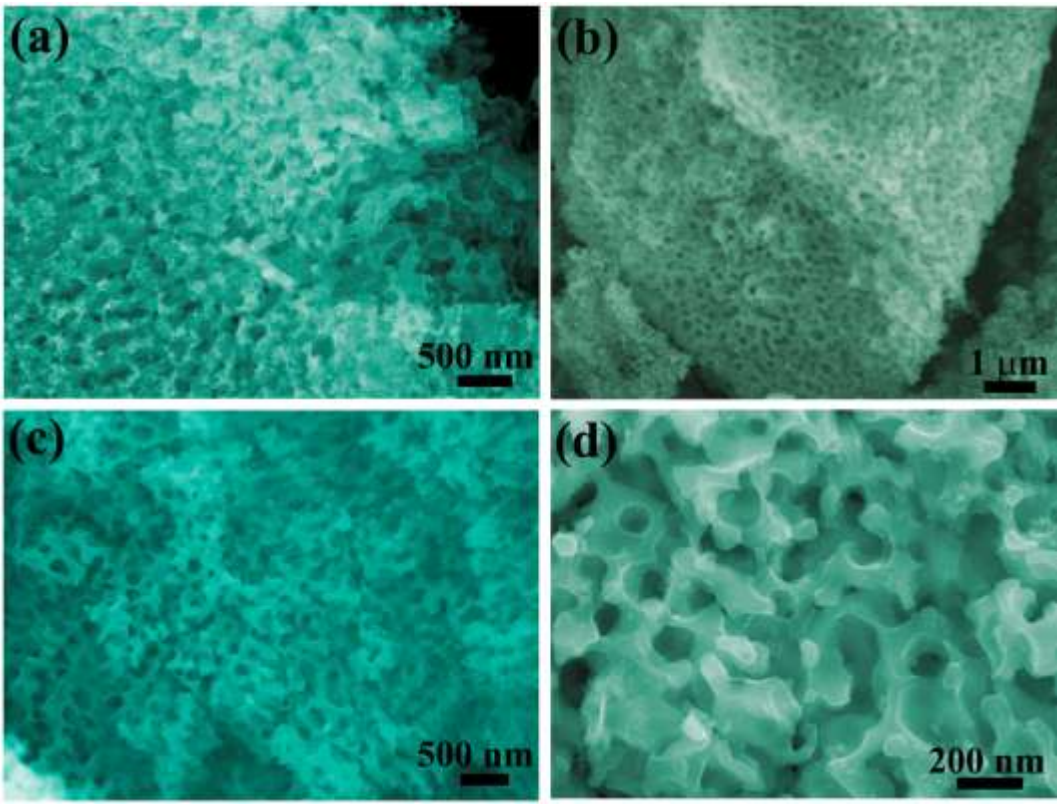

Fig. 4

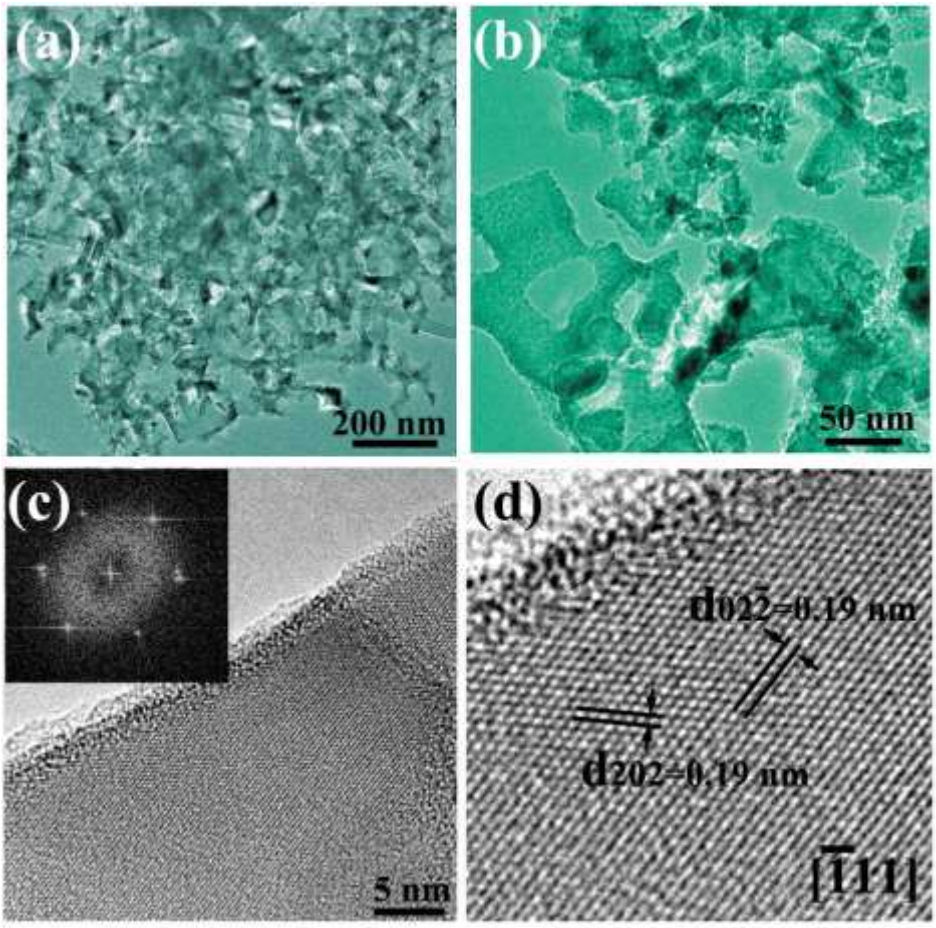

Fig. 5

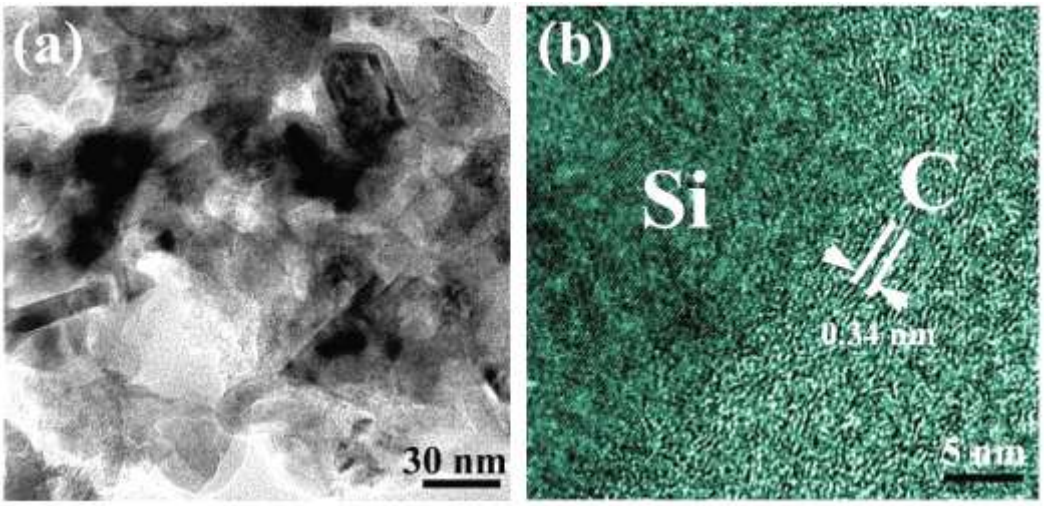

Schema 1

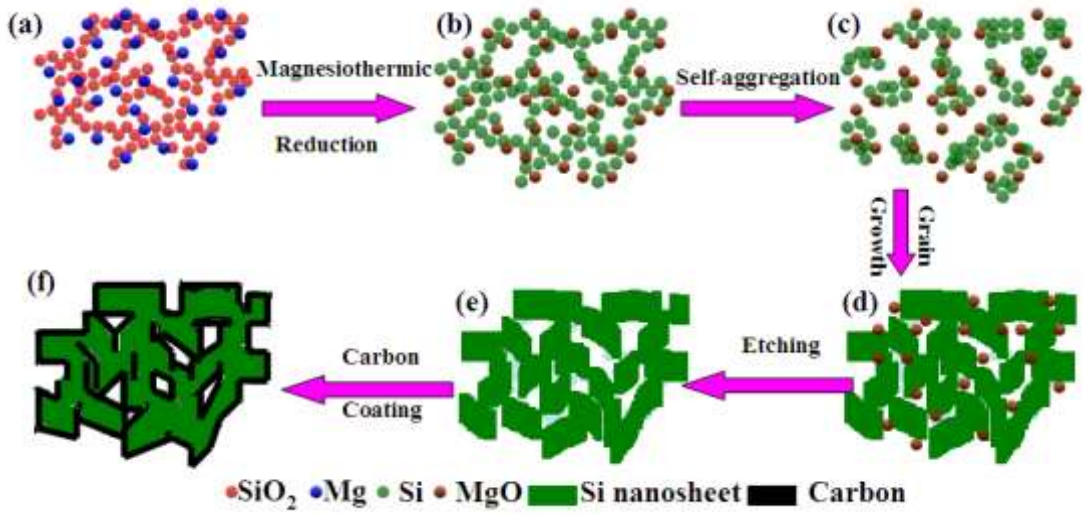

Fig. 6

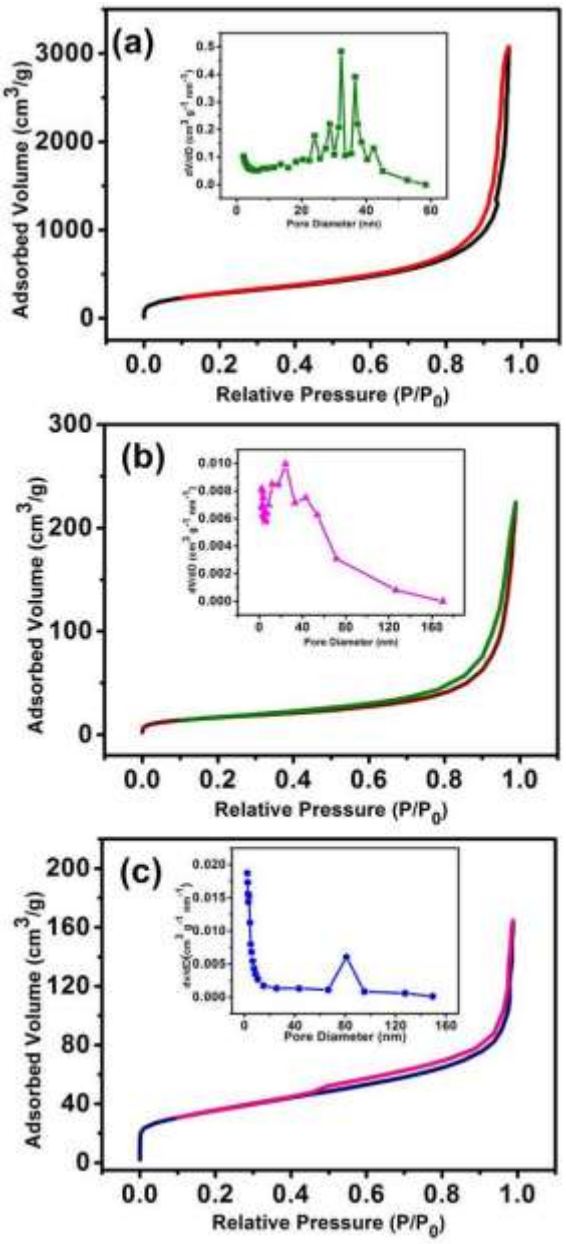

Fig. 7

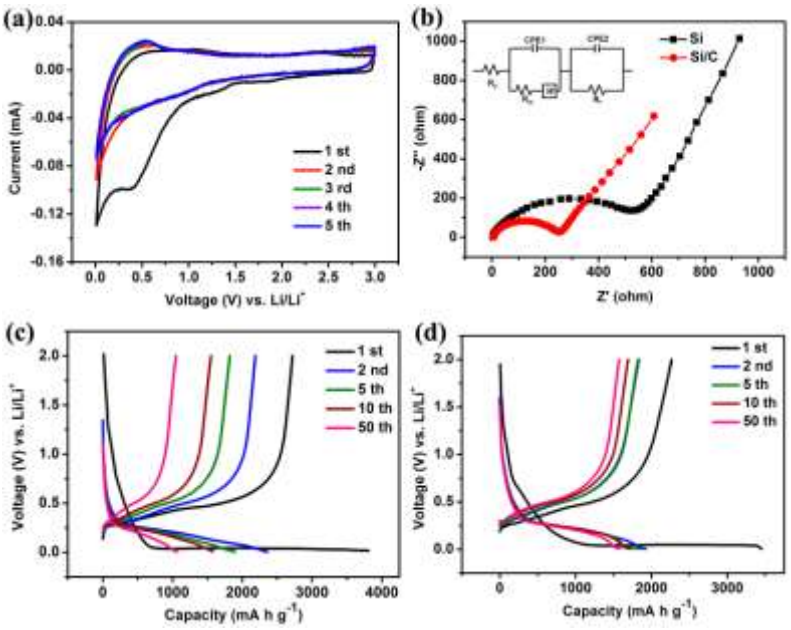

Fig. 8

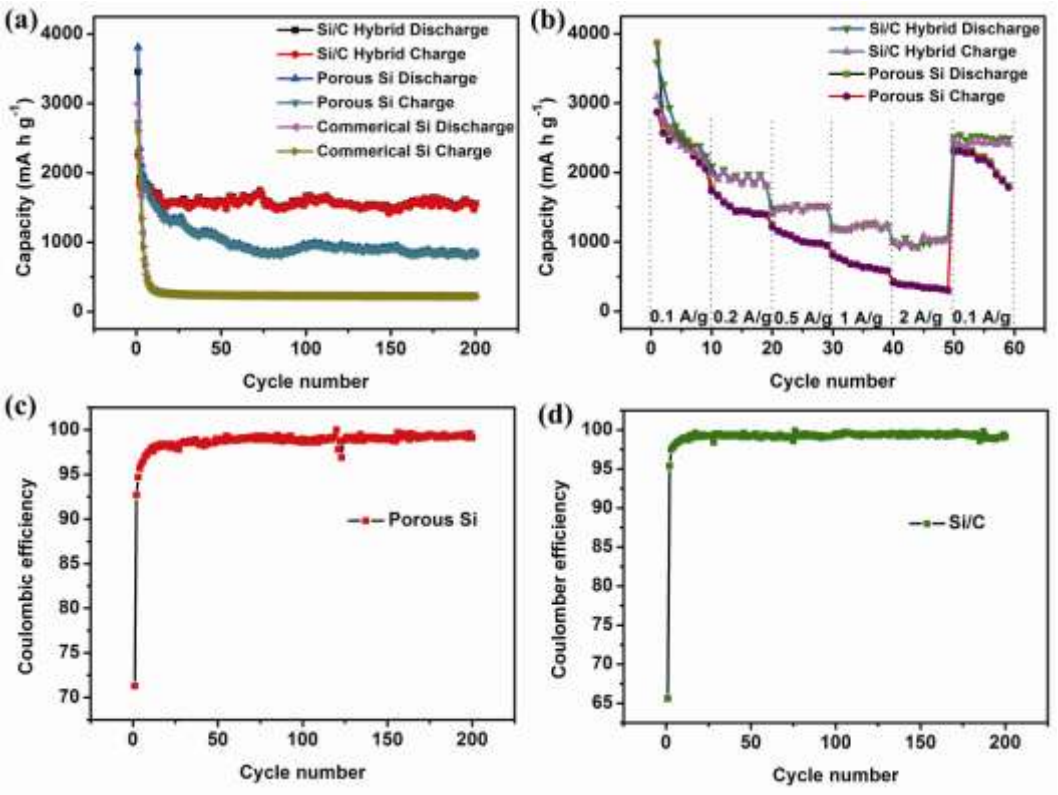

Schema 2

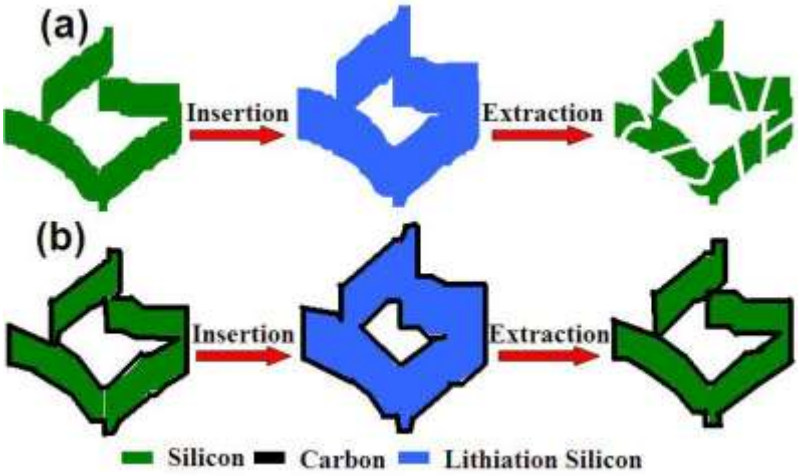

Table of Contents

A three dimensional interconnected porous silicon/carbon hybrid material is synthesized via a controllably magnesiothermic reduction route from silica aerogels and exhibits excellent lithium ion storage performance with long cycling life and perfect rate capability.